MR-based motion correction for PET imaging using wired active MR microcoils in simultaneous PET-MR: Phantom study[a)]

Chuan Huang
Center for Advanced Medical Imaging Sciences, Division of Nuclear Medicine and Molecular Imaging, Department of Imaging, Massachusetts General Hospital, Boston, Massachusetts 02114 and Department of Radiology, Harvard Medical School, Boston, Massachusetts 02115

Jerome L. Ackerman
Martinos Center for Biomedical Imaging, Massachusetts General Hospital, Charlestown, Massachusetts 02129 and Department of Radiology, Harvard Medical School, Boston, Massachusetts 02115

Yoann Petibon
Center for Advanced Medical Imaging Sciences, Division of Nuclear Medicine and Molecular Imaging, Department of Imaging, Massachusetts General Hospital, Boston, Massachusetts 02114

Thomas J. Brady, Georges El Fakhri, and Jinsong Ouyang[b)]
Center for Advanced Medical Imaging Sciences, Division of Nuclear Medicine and Molecular Imaging, Department of Imaging, Massachusetts General Hospital, Boston, Massachusetts 02114 and Department of Radiology, Harvard Medical School, Boston, Massachusetts 02115

(Received 20 September 2013; revised 20 February 2014; accepted for publication 26 February 2014; published 19 March 2014)

Purpose: Artifacts caused by head motion present a major challenge in brain positron emission tomography (PET) imaging. The authors investigated the feasibility of using wired active MR microcoils to track head motion and incorporate the measured rigid motion fields into iterative PET reconstruction.
Methods: Several wired active MR microcoils and a dedicated MR coil-tracking sequence were developed. The microcoils were attached to the outer surface of an anthropomorphic ^{18}F-filled Hoffman phantom to mimic a brain PET scan. Complex rotation/translation motion of the phantom was induced by a balloon, which was connected to a ventilator. PET list-mode and MR tracking data were acquired simultaneously on a PET-MR scanner. The acquired dynamic PET data were reconstructed iteratively with and without motion correction. Additionally, static phantom data were acquired and used as the gold standard.
Results: Motion artifacts in PET images were effectively removed by wired active MR microcoil based motion correction. Motion correction yielded an activity concentration bias ranging from −0.6% to 3.4% as compared to a bias ranging from −25.0% to 16.6% if no motion correction was applied. The contrast recovery values were improved by 37%–156% with motion correction as compared to no motion correction. The image correlation (mean ± standard deviation) between the motion corrected (uncorrected) images of 20 independent noise realizations and static reference was $R^2 = 0.978 \pm 0.007$ (0.588 ± 0.010, respectively).
Conclusions: Wired active MR microcoil based motion correction significantly improves brain PET quantitative accuracy and image contrast. © *2014 American Association of Physicists in Medicine*. [http://dx.doi.org/10.1118/1.4868457]

Key words: brain PET, motion correction, active microcoil, PET-MR

1. INTRODUCTION

Dementia is one of the biggest health problems facing human society now and in the foreseeable future. Early diagnosis of dementia can have a tremendous impact on the treatment for patients and their family members. Positron Emission Tomography (PET) is a powerful tool in early detection and treatment of dementia.[1] In addition to imaging metabolism in Alzheimer's disease (AD) using ^{18}F-FDG,[2] amyloid and tau radioligands have great potential in imaging AD as they bind with high affinity and specificity to the amyloid and tau structures which are the pathological hallmarks of the disease. PET scans can also be used to diagnose brain tumors and monitor recurrence after treatment. Furthermore, PET also plays an important role in neuroimaging of animal models of brain diseases.

Patient head motion during an imaging procedure can severely blur the reconstructed PET image if no correction is applied. One way to reduce head movement during a PET scan is to use head restraints such as thermoplastic masks, which are not able to completely eliminate the head movement but create significant discomfort or claustrophobia. Even with head restraints, typical translations in the range of 5–20 mm and rotations of 1°–4° are observed.[3] This is particularly true in elderly or pediatric patients, with increased significance in patients with dementia or movement disorders.

For animal research studies, forcibly restraining an animal can lead to significant perturbation of stress sensitive neurochemical processes in the brain.[4,5] Although anesthesia can be used to keep the animal still during a PET scan, previous studies showed that such approach may interfere with the neurological process under study.[6–9]

In the past, image based motion correction methods in brain PET imaging typically involve the division of a PET scan into a number of frames, followed by spatial registration and summing of the reconstructed PET images.[10–12] The motion correction can also be performed directly in the projection space.[13,14] These correction strategies (image space or projection) are likely inadequate for robust clinical usage because of the dependence on the noise characteristics of the PET data and the assumption that the activity distribution does not change significantly within the frames. Large errors can arise due to the spatial resolution of PET. In order to address these limitations, two methods using real-time measurements of motion were proposed in the past. One method was to use a video camera-based surveillance system with three light sources attached to the head and two cameras placed on the gantry of the PET scanner.[15,16] The other was to use a commercially available infrared optoelectronic motion-tracking device employing four IR-reflective spheres.[17] However, it is challenging to implement these methods in PET-MR systems because of lack of space in the scanners, the difficulty of maintaining line-of-sight between the optical targets and detectors, and the technical challenge related to MR compatibility.

Simultaneous PET-MR is a novel and promising imaging modality that is generating substantial interest in the medical imaging community, while offering many challenges and opportunities. Simultaneous PET-MR allows simultaneous measurement of anatomy, functionality, and *in vivo* biochemistry of tissues and cells. For brain imaging, the combined modalities may provide new insights in the fields of neuroscience and neurologic disorders as they can be used to simultaneously study brain function, metabolism, oxygen consumption, and perfusion.[18,19] Simultaneous PET-MR also makes it possible to perform MR-based motion correction for PET data.

The MR beam navigator pulse sequence, which can achieve less than 20 ms temporal resolution, is a conventional method to track motion.[20,21] However, due to the complex nature of head motion which includes both translation and rotation, the beam navigator method, which tracks only 1D motion, is not feasible for head motion monitoring. Other k-space MR navigators, such as the cloverleaf navigator,[22,23] solve this problem but their accuracy suffers from off-resonance effects, gradient instabilities, as well as signal contamination from nonrigid motion of the neck. Furthermore, the cloverleaf navigator requires approximately 20 s of motionless data to calibrate. Image-based MR motion tracking is also possible.[24] However, it generally lacks spatial resolution and temporal resolution because of the long scanning time needed for acquiring the image volume of the entire brain.

In this work, we propose and evaluate a novel approach to tackle the head motion problem in PET. We use wired active MR microcoils as markers to track head motion in real time during a brain PET acquisition. Wired active MR microcoils,[25] which have been used in MR to correct head motion during MR acquisition,[26–28] can measure head motion with submillimeter spatial accuracy and better than 15 ms temporal resolution. The motion measured by the wired active MR microcoils is incorporated into list-mode PET expectation maximization (EM) reconstruction. We use the term "wired active MR microcoil" to distinguish these coils from those which are not electrically connected to the scanner via cables ("wireless microcoils" or "inductively coupled wireless micro-coils").

2. MATERIALS AND METHODS

2.A. Phantom experiment

We performed a phantom experiment on a whole-body simultaneous PET-MR scanner. This scanner, a Siemens Medical Systems (Erlangen, Germany) Biograph mMR simultaneous PET-MR scanner, is composed of a 3T magnet (163 cm length; 60 cm bore), a whole-body gradient coil system, a radiofrequency (RF) body coil, and a PET system. The PET camera is installed between the gradient and the RF coil and operates in full 3D mode. The PET camera is composed of eight rings of 56 detector blocks composed of 8×8 lutetium oxyorthosilicate crystals ($4 \times 4 \times 20$ mm). The PET imaging field of view (FOV) is of 59.4×59.4 cm in transaxial (X-Y plane) direction and 25.8 cm in the axial (Z) direction. Six wired active MR microcoils were attached to the outer surface of a 3D Hoffman phantom (Data Spectrum Corporation, Hillsborough, NC) filled with 3.5 mCi ^{18}F. Complex motion including both translation and rotation was introduced by a ventilator-driven balloon and the slope of a wood container [shown in Fig. 1(a)]. When inflated by the ventilator, the balloon pushed the phantom up the slope. When the balloon was deflated, the phantom rolled down the slope; this results larger than 5 cm translation and approximately 30° rotation. Each motion cycle took approximately 2.5 s. During the acquisition, the phantom also drifted approximately 10 mm along the axial direction of the scanner. As a result, the introduced motion is not purely periodic.

First, 20 min of static PET list-mode data were acquired while the ventilator was turned off. Second, 32 min of dynamic PET data were acquired while the ventilator was turned on to introduce phantom motion. The 3D positions of the six wired active microcoils were tracked every 15 ms during the PET data acquisition.

2.B. Motion tracking using wired active MR microcoils

Wired active MR microcoils were used as markers to track the motion. As shown in Figs. 1(b) and 1(a), solenoidal MR microcoil was wound around a heat-sealed polyethylene tube (3.1 mm in diameter and 5 mm in length) containing deionized water doped with 1.25 g $NiSO_4 \bullet 6H_2O$ and 5 g NaCl per kg H_2O. The windings were formed from seven turns of 26 American Wire Gauge (AWG) magnet wire resulting in

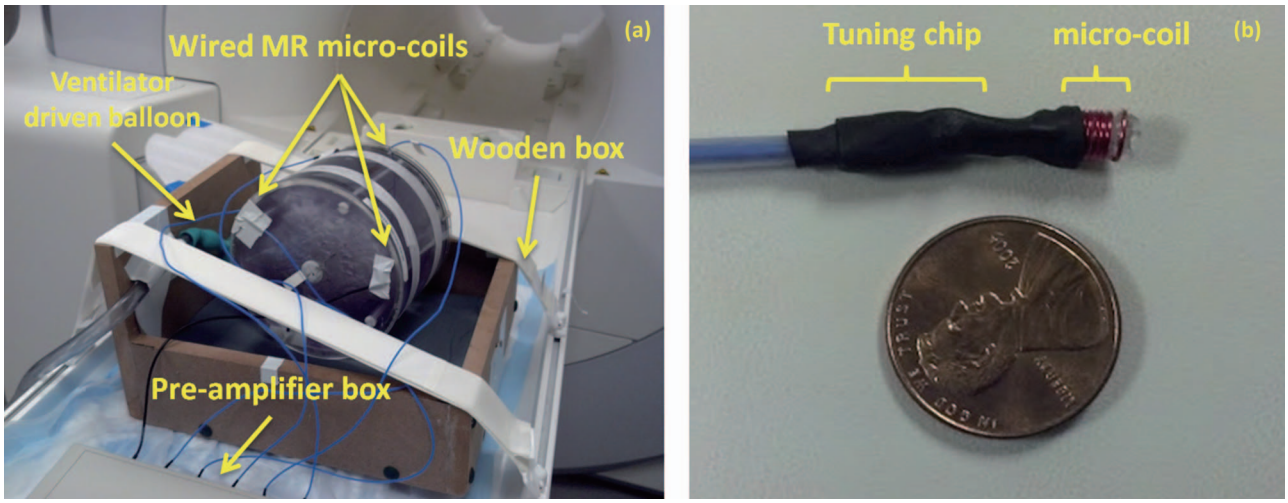

FIG. 1. (a) Experimental setup for the Hoffman phantom PET-MR experiment. (b) One of the six wired active MR microcoils used in the phantom experiment.

an inductance on the order of 130 nH and an effective RF series resistance on the order of 1.3 Ω. All six coils used in the phantom experiment were parallel tuned and series matched with Johanson type 9341 nonmagnetic SMD trimmer capacitors to 123.23 MHz (Larmor/resonance frequency of the 3T MR unit) and connected to individual channels of a six-channel preamplifier with 60 cm of Temp-Flex (South Grafton, MA) 50HCX-15 50 Ω Teflon dielectric nonmagnetic miniature coax cable (1.8 mm in diameter). The preamplifier inputs were protected with crossed diodes to limit the transmitter pulse power and cable traps to attenuate RF transmitted on the cable shields.

A dedicated MR pulse sequence (see Fig. 2) was developed to obtain real-time 3D locations of the wired active microcoils by measuring the projections of the microcoils. A gradient readout was performed along the X, Y, Z directions after a nonselective RF excitation pulse with small flip angle (1° in this work) was applied. For a given channel corresponding to a wired active microcoil, a bright signal appeared at the position corresponding to the location of the sample placed in the microcoil in the X, Y, Z projections. Another Free Induction Decay (FID) was also acquired with each set of projections to account for the local B_0 field variation A strong gradient was applied after each readout to dephase residual transverse magnetization. The real-time 3D positions of the wired active microcoils were determined with 15 ms temporal resolution (including the acquisition of X, Y, Z projections and the FID). The spatial resolutions of the projections were set to 2.1 mm in this work which is well below the approximately 4 mm PET spatial resolution. Better tracking spatial resolution can be achieved by adjusting the parameters. Because the phantom motion was rigid, its location and orientation could be uniquely determined using three or more noncollinear wired active microcoils. We selected the phantom location and orientation at which the static data were acquired (i.e., when the ventilator was turn off) as the reference motion phase. For each time point, a transformation matrix (a rotation and a translation) relative to the reference motion phase was obtained from the locations of three out of six wired active microcoils using a least-squares estimation algorithm developed by Arun *et al.*[29] Voxelwise motion fields across the entire FOV were generated using the transformation.

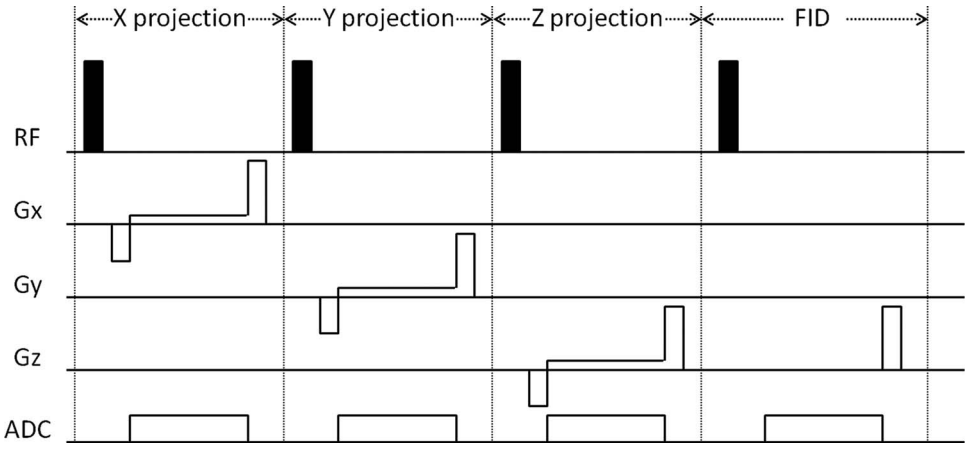

FIG. 2. The schematic plot of the MR wired active microcoil tracking pulse sequence module. Projections along X, Y, Z axes as well as a FID were acquired. This sequence module can measure the locations of all coils within 15 ms. In this work, the RF pulse flip angle was 1°.

2.C. Motion dependent attenuation map

The nonmoving attenuation map consists of all the hardware on the inner side of the PET detectors within the mMR gantry, the patient bed, and the wood box [see Fig. 1(a)]. The attenuation maps of the former two components were provided by the scanner. The attenuation map of the wood box was generated from a separate CT scan. Because wood is invisible in MR, in order to properly position the wood box in the attenuation map, several vitamin E capsules, which could be identified on both CT and MR images, were sealed inside the panels of the wood box. The CT image volume of the wood box was transformed so that the position of each capsule in the CT matched the corresponding position in the MR. The moving attenuation map of the Hoffman phantom was also derived from a CT scan. The CT image of the Hoffman phantom was initially aligned to the MR image acquired at the reference location using mutual information based registration.[30] Afterwards, the registered CT image was transformed to each motion phase using the motion tracked by the wired active microcoils to obtain the attenuation map at a given time point. The attenuation of the balloon, the tube connecting the balloon to the ventilator, and the wired active microcoils is negligible. The nonmoving and moving (i.e., the phantom) attenuation maps were then combined to obtain the overall PET attenuation map for a given motion phase.

2.D. PET reconstruction

Given the real-time 3D locations of the wired active microcoils, we binned all the dynamic PET events into M motion phases so that there is almost no motion within each phase. The phases of two different events are the same if

$$\left|\overrightarrow{r_i^k} - \overrightarrow{r_j^k}\right| < \beta \text{ for all k}, \tag{1}$$

where $\overrightarrow{r_i^k}$ and $\overrightarrow{r_j^k}$ are the 3D position of kth wired active microcoil ($k = 1, 2, \ldots, K$) for the ith and jth events, respectively, and β is a distance threshold. In this study, β was set to 2 mm, which is more than the tracking accuracy (<1 mm) but less than the spatial resolution of the PET scanner (approximately 4 mm at the center of FOV). The number of motion phases in the end will depend on the motion of the subject and the distance threshold β. In our phantom experiment, $\beta = 2$ mm led to roughly 100 motion phases. The list-mode ordinary Poisson EM algorithm, which was used in this work for reconstructing N events measured in M motion phases into a reference motion phase, can be formulated as follows:[31,32]

$$x_j^{k+1} = \frac{x_j^k}{\bar{s}_j} \sum_{n=1}^{N} a_{i_n,j}^m \frac{1}{\sum_{j'}^{J} a_{i_n,j'}^m x_{j'}^k + \overline{Sc}_n + \bar{R}_n}, \tag{2}$$

where x_j^k is the estimated activity in voxel j ($j = 1, 2, \ldots, J$) at the kth iteration, $a_{i_n,j}^m$ is an element of the motion-dependent system matrix representing the probability for a positron emission occurring in voxel j in motion frame m to be detected along line of response (LOR) i_n ($i_n = 1, 2, \ldots, I$, where I is the total number of LORs of the scanner), $\bar{s}_j$ is the average sensitivity for voxel j over all motion phases, and $\overline{Sc}_n$ and $\bar{R}_n$ are the average scatter and random estimates, respectively, along LOR i_n. The motion dependent system matrix is given by

$$A^m = \left(a_{i_n,j}^m\right)_{I\times J} = \boldsymbol{S}\boldsymbol{T}_m\boldsymbol{P}\boldsymbol{M}_m, m = 1, 2, \ldots, M; \tag{3}$$

where $\boldsymbol{M}_m$ of size $J \times J$ is the motion fields obtained from the wired active microcoils that can be used to transform the image volume at the reference motion phase to match the image volume at motion phase m. $\boldsymbol{P}$ of size $I \times J$ is the forward-projection matrix which can be calculated analytically using a ray-tracer algorithm.[33] Diagonal matrix $\boldsymbol{T}_m$ of size $I \times I$ provides the LOR dependent attenuation factors for motion phase m. Diagonal matrix $\boldsymbol{S}$ of size $I \times I$ provides the LOR dependent normalization factors. Since no periodic motion was assumed in the reconstruct technique shown here, this wired active microcoil based motion correction method is capable of correcting for any arbitrary motion.

It is impractical to compute the scatter and random corrections for more than 100 motion phases. Since those contributions are known to vary slowly with changing activity, they were computed for less than ten coarse motion phases using a larger distance threshold $\beta_c = 8$ mm. The $\overline{Sc}_n$ and $\bar{R}_n$ were calculated separately in each coarse motion phase and averaged over all the phases weighted by the duration of the corresponding phase. Similarly, the sensitivity image volume was computed using the coarse motion phases. For the sake of computation time, the sensitivity matrix was also calculated using the coarse motion frames.

The dynamic PET list-mode data with 6.3×10^9 counts were binned into 20 temporal noise realizations. Each noise realization was reconstructed with the following two methods:

(1) nMC: All the events in the noise realization were used in the reconstruction without motion correction. The attenuation map at the reference motion phase was used.
(2) MC: All the PET events in the noise realization were reconstructed into the reference motion phase by applying the motion correction algorithm described above. Motion dependent attenuation maps were used.

Additionally, the static PET data set, which has 2.6×10^9 counts, was reconstructed as the gold standard (STATIC).

All the images were reconstructed with ten iterations and eight temporal subsets on a $4.17 \times 4.17 \times 2$ mm voxel grid. No postreconstruction smoothing filter was applied. A schematic diagram of the MR wired active microcoil based motion correction algorithm is shown in Fig. 3.

2.E. Quantitative assessment

To objectively assess the image quality of the motion corrected images, we performed the following three studies:

(1) Image/profile similarity: To quantitatively assess the performance of our motion correction method, the correlation coefficient (R^2, square of Pearson correlation coefficient), which quantifies the image similarity between the static reference and reconstructed image

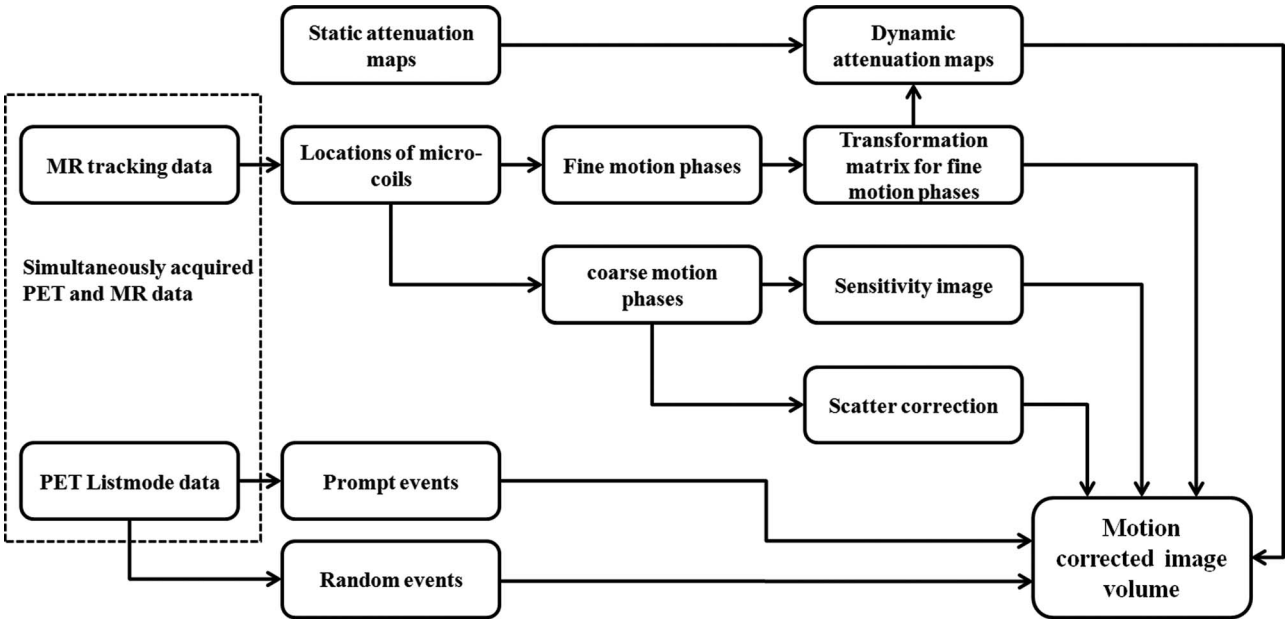

FIG. 3. A schematic diagram of the MR microcoil based motion-correction algorithm.

with or without motion correction, was computed for each noise realization.

(2) Activity concentration bias: We defined five activity-present ROIs in the Hoffman phantom corresponding to the location of the following structures: posterior cingulate (ROI 1), anterior cingulate (ROI 2), caudate (ROI 3), striatum (ROI 4), and thalamus (ROI 5). For both nMC and MC, bias of the normalized activity concentration for each noise realization was calculated using

$$b_i^k = \frac{z_i^k - z_i^S}{z_i^S}, \tag{4}$$

where z_i^k is the average activity concentration in ROI i for noise realization k, and z_i^S is the average activity concentration in ROI i for STATIC. Afterwards, we computed the mean and standard deviation of bias across all the noise realizations.

(3) Contrast recovery: For each of the five ROIs defined above, an activity-absent ROI was defined in the nearby background region. For the ith activity-present and activity-absent ROI pair, we computed the contrast recovery for noise realization k using

$$c_i^k = 1 - \frac{z_{i(a)}^k}{z_{i(p)}^k}, \tag{5}$$

where $z_{i(a)}^k$ and $z_{i(p)}^k$ is the average activity concentration in activity-absent and activity-present, respectively, for noise realization k. We then computed the mean and standard deviation of the activity concentration ratio across all the noise realizations.

3. RESULTS

Figure 4 shows the X, Y, Z projections of the sample within a moving wired active microcoil versus time. Because each coil was connected to a separate channel, the spatial locations of all the coils can be determined simultaneously by the wired active microcoil tracking pulse sequence. It can be seen that the signal intensity changed with time. This is because the sensitivity of the wired active microcoil was affected by its orientation with respect to the static magnetic field of the scanner. The location estimation, however, was not affected.

The top panel of Fig. 5 shows three slices in three different views for STATIC, nMC, and MC (one noise realization each for nMC and MC). Without the wired active microcoil based motion correction, the motion artifacts are prominent. The artifacts caused by the mismatch between the dynamic emission data and the static attenuation map are also visible. Our motion correction approach removed the severe motion artifacts and yielded images very similar to STATIC. Since the number of events used in STATIC is much larger than the number of events used for the MC reconstruction, the

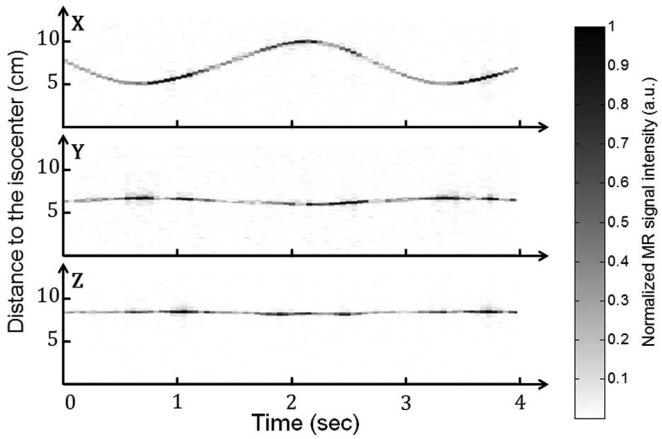

FIG. 4. The projections of the sample within one of the moving wired active microcoils along X, Y, and Z axes versus time. The gray scale values of the curves reflect the varying MR intensity.

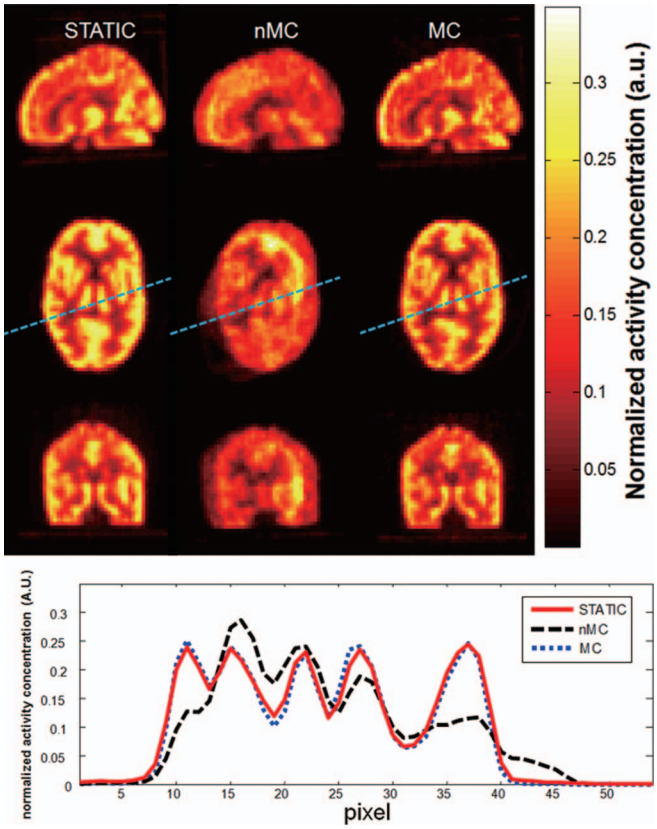

FIG. 5. (Top) Sagittal, axial, and coronal views for STATIC, nMC, and MC for one noise realization. For nMC and MC, the images were reconstructed for one noise realization, which includes 1.6 min of PET data. (Bottom) The profiles along the dashed lines for STATIC, nMC, and MC of this noise realization.

MC images are noisier. The similarity of the reconstructed PET image volumes was studied by calculating correlation coefficients. Correlation coefficients were calculated between STATIC and MC (and nMC) for each noise realization. The STATIC-MC and STATIC-nMC correlation coefficient is $R^2 = 0.978 \pm 0.007$ (mean $\pm$ standard deviation), and $R^2 = 0.588 \pm 0.010$, respectively. As shown in the bottom panel of Fig. 5, MC yielded profiles similar to STATIC but very different from nMC. The similarity of the line profiles was also quantified by correlation analysis: the correlation coefficient between MC and STATIC for this noise realization is $R^2 = 0.991$, while the correlation coefficient between nMC and STATIC is $R^2 = 0.734$.

Figure 6(a) shows the mean and standard deviation of the activity concentration bias computed over all the noise realizations in each of the five ROIs. As expected, the activity concentrations obtained by MC coincide well with STATIC, while large biases are observed in the activity concentration calculated using the nMC images. The absolute bias ranges from -25.0% to 16.6% and -0.6% to 3.4% for nMC and MC, respectively.

Figure 6(b) shows the contrast recovery computed using Eq. (5) for the same five ROIs. If the motion artifacts are not compensated, the contrast recovery values of these structures are significantly lower as compared to MC and STATIC. MC yielded contrast recovery values similar to STATIC. As compared to nMC, MC improved the contrast recovery [the improvement is defined as $(\overline{c_i^{\mathrm{MC}}} - \overline{c_i^{\mathrm{nMC}}})/\overline{c_i^{\mathrm{nMC}}}$, where $\overline{c_i^{\mathrm{nMC}}}$ and $\overline{c_i^{\mathrm{MC}}}$ are, respectively, the mean contrast recovery values of nMC and MC for ROI i as show in Fig. 6(b)] value by 156%, 48%, 84%, 67%, and 37% for ROI 1–5, respectively ($p < 10^{-5}$ for every ROI with 20 noise realizations).

4. DISCUSSION

The minimal number of wired active microcoils needed to track the motion of the head is three. However, more wired active microcoils make the motion estimation more accurate and reliable. The motion of the phantom in this study, which is larger than 5 cm in translation and 30° in rotation, is significantly larger and faster than the head motion normally expected in clinical practice. However, such large and fast motion may be encountered when imaging dementia or pediatric patients.

We were able to track head motion with 15 ms temporal resolution. Given the fact that the motion of the head is much less frequent in most clinical scans, the sequence module for wired active microcoil tracking could be interleaved every few

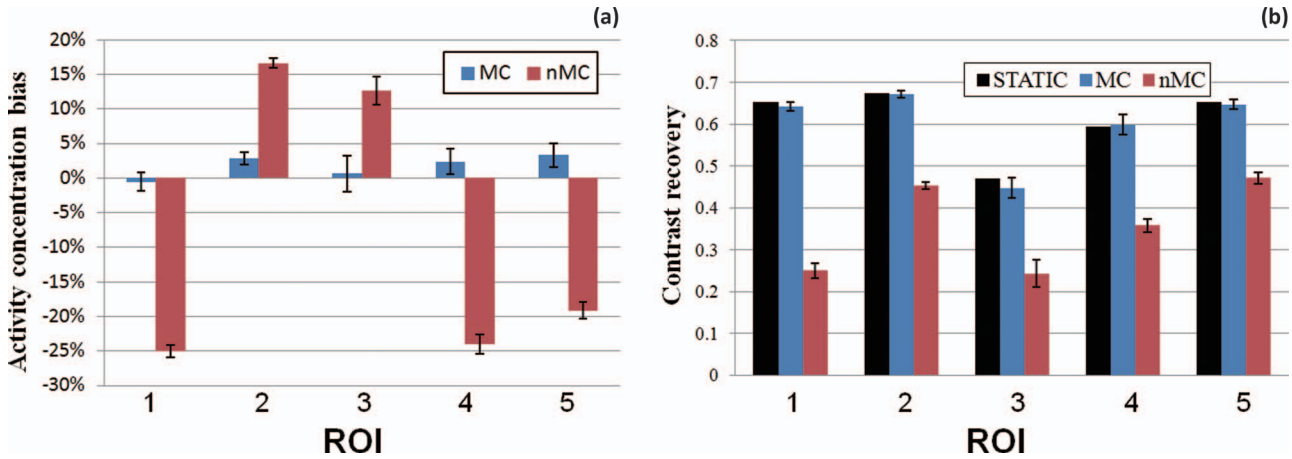

FIG. 6. (a) Activity concentration biases of ROIs drawn inside the phantom. (b) The contrast recovery values for the same five ROIs.

seconds with other MR scans. In this way, motion information can be acquired while other clinical MR sequences are being performed. Because a very small (1°) flip angle was used and because the duration of the tracking module is short, the wired active MR microcoil tracking pulse sequence module can be incorporated into most clinical sequences (for example, gradient-echo, spin-echo, and echo-planar, the workhorses of clinical brain MRI) with minimal impact on image quality. For some sequences, for example, steady-state free precession, incorporation of wired active microcoil tracking will be more challenging. The wired active microcoil tracking rate can potentially be determined by the operator based on how rapid, extensive, or frequent the motion is.

The MR sequence module implemented in this work can obtain the locations of multiple wired active microcoils in approximately 15 ms. To achieve faster update rate, instead of using four RF excitations (see Fig. 1), one excitation can be used and the three projections can be obtained using multiple gradient echoes. Temporal resolution <5 ms can be achieved using a k-space trajectory similar to cloverleaf navigator.[23] Although a 5 ms temporal resolution for motion tracking may not be necessary for tracking head motion, the short duration of the tracking sequence module and the use of miniscule RF flip angle imply minimal impact upon the host MR sequence.

The spatial resolution of the tracking sequence module used in this work was 2.1 mm. However, depending on the application (such as small animal studies), much higher spatial resolution can be easily achieved by changing the matrix size and the size of the imaging FOV.

In clinical practice, three widely separated wired active microcoils can be mounted on a head band or a MR-compatible eyeglass frame[34] to track the head motion. The motion measured by wired active MR microcoils can be used for PET motion correction including motion dependent MR-based PET attenuation correction. Also, on Siemens mMR PET-MR scanners, a Dixon-based attenuation correction (MRAC) pulse sequence is used to acquire MR images, which are in turn used to generate the PET attenuation map. Head motion is possible during the MRAC acquisition, which can last for 20 s. Since MRAC is a gradient-echo based sequence, the microcoil based tracking pulse sequence module can be added to it to allow prospective motion correction during the MRAC acquisition[27] so that an accurate PET attenuation map can be obtained. Because of the fast update rate of wired active microcoil based motion tracking, the measured motion can be incorporated into both structural MRI and fMRI sequences to perform prospective real-time motion compensation for brain imaging. The proposed approach requires minimal additional hardware and can be integrated with the standard user interface, allowing transferability to clinical practice.

In this study, we used the integrated RF body coil to excite the samples within all the wired active microcoils. This can cause RF heating of the cables, especially at the cable ends. In the future, we plan to use the wired active microcoils for both transmitting and receiving. This makes the additional RF power deposition from the microcoils close to zero. Also, triaxial cables and RF traps similar to what are used in commercial RF coils will be used to reduce the potential cable heating effect. MR safety test of the microcoils will be conducted before using these on subjects. Furthermore, coil tuning and signal quality will be much less sensitive to positioning and proximity to various structures or tissue.

Recently, there has been an increased interest in inductively coupled wireless coils[35,36] in the MR community. Inductively coupled wireless coils are "connected" to the MR scanner inductively via the integrated body RF coil, and operate in transmit/receive mode (the coils excite the spins of the self-contained marker sample and also act as local receive coils). As compared to wired active microcoils, inductively coupled wireless microcoils are more patient friendly and do not require preamps. However, unlike wired active microcoils, each inductively coupled wireless microcoil does not have its own receiver channel. It is challenging to distinguish each individual microcoil when multiple microcoils are used, although solutions to this problem have been reported.[36]

Besides the proposed wired active microcoil based motion correction, several other approaches have been investigated previously by other groups. In PET image based motion correction, PET events are divided into multiple frames and PET reconstruction is performed for each frame. The motion fields are then obtained by spatial registration between the reconstructed image volumes. This method is limited by noise and PET spatial resolution. The motion fields can also be obtained by registering MR image volumes acquired at different times. This method is limited by the tradeoff between temporal and spatial resolution of the MR imaging. Therefore, we expect that our approach outperforms both PET and MR image based methods. Real-time motion tracking using optical devices has been studied on PET-CT scanners with performance equivalent to our approach.[3] However, it is challenging to use such systems for PET-MR because the MR head coil could block the optical paths in the highly confined space within the scanner bore, not to mention magnetic and RF compatibility problems posed by optical devices. Catana *et al.*[22] performed a Hoffman phantom study using a brain PET-MR prototype (brainPET). The phantom was placed at five different positions during the data acquisition. A slow multiecho magnetization-prepared rapid acquisition gradient echo sequence (ME-MPRAGE) was used for MR imaging. They also performed patient studies using a cloverleaf MR navigator sequence, which has 20 ms temporal resolution, for motion tracking. PET activity in three different brain structures computed with and without MR-based motion correction was plotted versus time for four consecutive 3-min frames. The results obtained using our approach appears to be equivalent to their phantom results. As compared to their patient results, the bias and standard deviation we obtained appears to be lower. One possible source of this could be the MR k-space signal contamination caused by the nonrigid motion of the neck, to which our wired active microcoil based motion correction technique is immune.

In the future, we plan to perform patient studies by attaching multiple wired active microcoils to a headband or eyeglass

frame[35] after approval by our Institutional Review Board. We will scan the subjects while motionless and while intentionally moving. We will evaluate the performance of our MR microcoil based motion correction approach using the motionless data as the reference.

5. CONCLUSION

In this work, we have proposed and validated a novel motion tracking and correction technique for PET imaging using MR microcoils in simultaneous PET-MR. Our MR wired active microcoil based motion correction yielded significantly improved PET image quality. It provides a solution to the well known motion problem in brain imaging.

ACKNOWLEDGMENTS

This research was supported in part by NIH Grant Nos. R21-EB012326, R01-CA165221, the Athinoula A. Martinos Center for Biomedical Imaging, and the Center for Functional Neuroimaging Technologies (funded by NIH/NIBIB Grant No. P41-EB015896).

[a)]This work was presented in part in the Society of Nuclear Medicine and Molecular Imaging 2013 Annual Meeting.
[b)]Author to whom correspondence should be addressed. Electronic mail: ouyang.jinsong@mgh.harvard.edu

[1]L. Mehta and S. Thomas, "The role of PET in dementia diagnosis and treatment," Appl. Radiol. **41**, 8–15 (2012).
[2]S. Minoshima, K. A. Frey, R. A. Koeppe, N. L. Foster, and D. E. Kuhl, "A diagnostic approach in Alzheimer's disease using three-dimensional stereotactic surface projections of fluorine-18-FDG PET," J. Nucl. Med. **36**, 1238–1248 (1995).
[3]P. Bloomfield, T. Spinks, J. Reed, L. Schnorr, A. Westrip, L. Livieratos, R. Fulton, and T. Jones, "The design and implementation of a motion correction scheme for neurological PET," Phys. Med. Biol. **48**, 959–978 (2003).
[4]B. Fueger, J. Czernin, I. Hildebrandt, C. Tran, B. Halpern, D. Stout, M. Phelps, and W. Weber, "Impact of animal handling on the results of ^{18}F-FDG PET studies in mice," J. Nucl. Med. **47**, 999–1006 (2006).
[5]A. Arnsten, "Stress impairs prefrontal cortical function in rats and monkeys: Role of dopamine D1 and norepinephrine alpha-1 receptor mechanism," Prog. Brain Res. **126**, 183–192 (2000).
[6]U. Lindauer, A. Villringer, and U. Dirnagl, "Characterization of CBF response to somatosensory stimulation: Model and influence of anesthetics," Am. J. Physiol. **264**, H1223–H1228 (1993).
[7]A. Angel, D. Linkens, and C. Ting, "Estimation of latency changes and relative amplitudes in somatosensory evoked potentials using wavelets and regression," Comput. Biomed. Res. **32**, 209–251 (1999).
[8]K. Hendrich, P. Kochanek, J. Melick, J. Schiding, K. Statler, D. Williams, D. Marion, and C. Ho, "Cerebral perfusion during anesthesia with fentanyl, isoflurane, or pentobarbital in normal rats studies by arterial spin-labeled MRI," Magn. Reson. Med. **46**, 202–206 (2001).
[9]Y. Nakao, Y. Itoh, T. Kuang, M. Cook, J. Jehle, and L. Sokoloff, "Effects of anesthesia on functional activation of cerabral blood flow and metabolism," Proc. Natl. Acad. Sci. U.S.A. **98**, 7593–7598 (2001).
[10]R. Woods, S. Cherry, and J. Mazziotta, "Rapid automated algorithm for aligning and reslicing PET images," J. Comput. Assist. Tomogr. **16**, 620–633 (1992).
[11]K. Friston *et al.*, "Spatial registration and normalization of images," Human Brain Mapp. **3**, 165–189 (1995).
[12]L. Tellmann *et al.*, "Concepts of registration and correction of head motion in positron emission tomography," Z. Med. Phys. **16**, 67–74 (2006).
[13]B. Hutton *et al.*, "A hybrid 3-D reconstruction/registration algorithm for correction of head motion in emission tomography," IEEE Trans. Nucl. Sci. **49**, 188–194 (2002).
[14]A. Kyme *et al.*, "Practical aspects of a data-driven motion correction approach for brain SPECT," IEEE Trans. Med. Imaging **22**, 722–729 (2003).
[15]Y. Picard and C. Thompson, "Motion correction of PET images using multiple acquisition frames," IEEE Trans. Med. Imaging **16**, 137–144 (1997).
[16]S. Goldstein *et al.*, "A head motion measurement system suitable for emission computed tomography," IEEE Trans. Med. Imaging **16**, 17–27 (1997).
[17]B. Lopresti *et al.*, "Implementation and performance of an optical motion tracking system for high resolution brain PET imaging," IEEE Trans. Nucl. Sci. **46**, 2059–2067 (1999).
[18]L. Thurfjell *et al.*, "Combination of biomarkers: PET [18F]flutemetamol imaging and structural MR in dementia and mild cognitive impairment," Neurodegenerative Dis. **10**, 246–249 (2012).
[19]M. Albert, C. DeCarli, and S. DeKosky, "The use of MRI and PET for clinical diagnosis of dementia and investigation of cognitive impairment: A consensus report," Alzheimer's Association Neuroimaging Work Group Consensus Report No. (available URL: http://www.alz.org).
[20]R. L. Ehman and J. Felmlee, "Adaptive technique for high-definition MR imaging of moving structures," Radiology **173**, 255–263 (1989).
[21]Y. Wang, R. C. Grimm, J. P. Felmlee, S. J. Riederer, and R. L. Ehman, "Algorithms for extracting motion information from navigator echoes," Magn. Reson. Med. **36**, 117–123 (1996).
[22]C. Catana, T. Benner, A. van der Kouwe, L. Byars, M. Hamm, D. B. Chonde, C. J. Michel, G. El Fakhri, M. Schmand, and A. G. Sorensen, "MRI-assisted PET motion correction for neurologic studies in an integrated MR-PET scanner," J. Nucl. Med. **52**, 154–161 (2011).
[23]A. J. van der Kouwe, T. Benner, and A. M. Dale, "Real-time rigid body motion correction and shimming using cloverleaf navigators," Magn. Reson. Med. **56**, 1019–1032 (2006).
[24]N. White, C. Roddey, A. Shankaranarayanan, E. Han, D. Rettmann, J. Santos, J. Kuperman, and A. Dale, "PROMO: Real-time prospective motion correction in MRI using image-based tracking," Magn. Reson. Med. **63**, 91–105 (2010).
[25]J. Ackerman, M. Offutt, R. Buxton, and T. Brady, "Rapid 3D tracking of small RF coils," Proc. Soc. Magn. Reson. Med. **5**, 1131–1132 (1986).
[26]L. Qin, E. J. Schmidt, Z. T. Tse, J. Santos, W. S. Hoge, C. Tempany-Afdhal, K. Butts-Pauly, and C. L. Dumoulin, "Prospective motion correction using tracking coils," Magn. Reson. Med. **69**, 749–759 (2013).
[27]M. B. Ooi, S. Krueger, W. J. Thomas, S. V. Swaminathan, and T. R. Brown, "Prospective real-time correction for arbitrary head motion using active markers," Magn. Reson. Med. **62**, 943–954 (2009).
[28]M. B. Ooi, S. Krueger, J. Muraskin, W. J. Thomas, and T. R. Brown, "Echo-planar imaging with prospective slice-by-slice motion correction using active markers," Magn. Reson. Med. **66**, 73–81 (2011).
[29]K. S. Arun, T. S. Huang, and S. D. Blostein, "Least-squares fitting of two 3-D point sets," IEEE Trans. Pattern Anal. Mach. Intell. **PAMI-9**, 698–700 (1987).
[30]D.-J. Kroon and C. H. Slump, "MRI modality transformation in demon registration," IEEE Int. Symp. Biomed. Imaging, 963–966 (2009).
[31]Y. Petibon, J. Ouyang, X. Zhu, C. Huang, T. Reese, Q. Li, and G. El Fakhri, "Cardiac motion compensation and resolution modeling in simultaneous PET-MR: A cardiac lesion detection study," Phys. Med. Biol. **58**, 2085–2102 (2013).
[32]S. Y. Chun, T. G. Reese, J. Ouyang, B. Guerin, C. Catana, X. Zhu, N. M. Alpert, and G. El Fakhri, "MRI-based nonrigid motion correction in simultaneous PET/MRI," J. Nucl. Med. **53**, 1284–1291 (2012).
[33]R. L. Siddon, "Fast calculation of the exact radiological path for a three-dimensional CT array," Med. Phys. **12**, 252–255 (1985).
[34]M. B. Ooi, M. Aksoy, J. Maclaren, R. D. Watkins, and R. Bammer, "Prospective motion correction using inductively coupled wireless RF coils," Magn. Reson. Med. **70**, 639–647 (2013).
[35]M. B. Ooi, M. Aksoy, J. Maclaren, R. D. Watkins, and R. Bammer, "Prospective rigid-body motion correction using miniature wireless RF-coils as position tracking probes," Proc. Int. Soc. Magn. Reson. Med. **21**, 305 (2013).
[36]S. Sengupta, S. Tadanki, J. C. Gore, and E. B. Welch, "Prospective real-time head motion correction using inductively coupled wireless NMR probes," Magn. Reson. Med. (in press).